Applied Ocean Research 134 (2023) 103493

Contents lists available at ScienceDirect

Applied Ocean Research

journal homepage: www.elsevier.com/locate/apor

Sloshing-induced motions of a spar inside a cylindrical dock with baffles in waves

Maël Moreau [a,*], Trygve Kristiansen [a], Babak Ommani [b], Bernard Molin [a,c]

[a] Norwegian University of Science and Technology (NTNU), Trondheim NO 7491, Norway
[b] SINTEF Ocean, 7450 Trondheim, Norway
[c] Aix-Marseille Université, CNRS, Centrale Marseille, IRPHE, Marseille 13013, France

A B S T R A C T

The motions of a free floating offshore wind turbine's (OWT) spar-type platform inside a bottom-less moored cylindrical dock are investigated for incident wave frequencies near the first lateral sloshing resonance, focusing on surge on pitch motions. The radiation and diffraction problems of the two-body system are first solved through a domain decomposition (DD) approach under linear potential flow assumptions. This semi-analytical model is extended to include the effects of solid and perforated baffles in the annular domain between the dock and the spar, adapting the method developed in our previous paper for the dock alone. Results are compared with those obtained with model tests, performed at scale 1:100 for both regular waves with low steepnesses and irregular sea states. The resonant peak amplitudes of the spar's surge and pitch motions are reduced by almost half when a solid baffle is installed, with a strong dependency on the incident wave height due to viscous dissipation caused by the flow separation at the sharp edge of the baffle.

1. Introduction

Transitions from fossil fuel-based electricity generation to cleaner forms of production have been strongly encouraged by the Intergovernmental Panel on Climate Change to help reaching Paris agreement's objectives (cf. Shukla et al., 2022), in particular to limit the temperature increase below 2 °C from pre-industrial times. The offshore wind turbine (OWT) industry has been pointed out as one of the most promising, with high technical potential that could provide several times the national needs in electricity for a large number of countries (cf. IEA, 2019). It is especially true for deep waters (above 50–60 m), where the technical potential is estimated to be about 3.8 times higher than for shallower waters. The installation of OWT in deep waters requires the use of floating platforms, either semi-submersibles, tensions leg platforms, or spar types. In 2017 the first farm of floating OWTs was installed along the coast of Scotland. Five Hywind spar-type OWTs of 6 MW each developed by Equinor (cf. Skaare, 2017) were assembled in a protected area near Stavanger, Norway, and then towed to site at 25 km from the coast of Scotland. In order to reduce installation costs, Equinor proposed the concept of a large circular cylindrical floating dock of 80 m diameter with an open bottom, referred in this paper as the dock, sheltering a calm water area inside from which the spar-type floating OWTs could be assembled directly on site (cf. Jiang et al., 2020). In our previous publication (cf. Moreau et al., 2022), we showed that non-negligible sloshing waves could develop inside the floating dock at operational sea-state conditions, caused by the surge and pitch motions of the structure exposed to incident waves. We proposed damping devices to reduce their amplitude when there was no OWT's spar inside. A semi-analytical method was developed to study the motions of the dock when both solid and perforated thin annular baffles were fixed on the internal wall of the structure, below the free surface. Effects of the baffles were modeled by introducing locally a quadratic viscous damping coefficient and a shifted natural sloshing period in the free-surface boundary condition. The motions were then compared to experimental results, showing a good agreement as long as the baffle's width was lower than the distance between the baffle and the free surface.

The presence of a free-floating OWT's spar inside the dock affects the natural sloshing modes. Because the draughts of both the spar and the dock are almost as high as incident wave lengths, natural eigen modes are then comparable to those of an annular tank with closed bottom. These sloshing modes were for example derived by Faltinsen and Timokha (2016), who investigated linear and non-linear sloshing resonances in an upright annular tank through multi-modal analysis. Linear modes in an annular tank were also studied thoroughly by Yue et al. (2018), using sloshing resonance as a damping system for seismic applications. Choudhary and Bora (2017) considered a rigid lid covering partially the free surface of the annular tank, pointing out a sharp increase of the first natural sloshing frequency as a function of increasing width of the lid. Their work, however, did not include

* Corresponding author.
E-mail address: mael.k.i.moreau@ntnu.no (M. Moreau).

https://doi.org/10.1016/j.apor.2023.103493
Received 6 October 2022; Received in revised form 8 February 2023; Accepted 11 February 2023
Available online 1 March 2023

Nomenclature

C_D	[–] Drag coefficient
C_M	[–] Mass coefficient
$F^{(k)}$	[N] or [N m] Exciting force or moment
F_5^M	[N m] Pitch moment on the baffle
F_D	[N] Heuristic drag load in surge
H_s	[m] Significant wave height
$I_{5,5}^{(k)}$	[kg m^2] Body's moment of inertia in pitch
J_p	[–] Bessel function of the first kind
$M^{(k)}$	[kg] Body's mass
N_I to N_V	Number of eigenfunctions kept in each subdomain I to V
$Or\theta z$	Cylindrical coordinates
$Oxyz$	Cartesian coordinates
$S_0^{(k)}$	[m^2] Body's mean wetted surface
S_x	[m^2 s] or [rad^2 s] Power spectral density
T	[s] Wave period
T_1	[s] Highest lateral sloshing natural period
T_N	[s] Natural periods from decay tests
T_p	[s] Peak period
T_{piston}	[s] Piston mode's natural period
Y_p	[–] Bessel function of the second kind
a	[m] Dock's inner radius
a_0	[m] Spar's radius
a_B	[m] Baffle's width
$a_{i,j}^{(k)}$, $d_{i,j}^{(k)}$	[kg] Added mass coefficients
b	[m] Dock's outer radius
$b_{i,j}^{(k)}$, $e_{i,j}^{(k)}$	[kg/s] Radiation damping coefficients
$c-b$	[m] Bilge box's width
$c_{i,j}^{(k)}$, $f_{i,j}^{(k)}$	[kg/s^2] Restoring coefficients
$d+s$	[m] Dock's draught
d_0	[m] Spar's draught
d_B	[m] Baffle's submergence
g	[m/s^2] Gravitational acceleration
h	[m] Water depth
k	[rad/m] Wave number
s	[m] Bilge box's height
t	[s] Time
$z_G^{(k)}$	[m] Body's vertical location of the centre of gravity
Ω	[m^3] Domain
$\boldsymbol{\Phi}$	[m^2/s] Potential flow
$\Psi_{p,q}$	[m/s] Radial sloshing eigenfunction
$\tilde{\eta}_j^{(k)}$	[m] or [rad] Motion's complex amplitude
$\boldsymbol{n}^{(k)}$	[–] Unit vector pointing outward the body (k)
$\boldsymbol{r}$	[m] Position vector
ϵ	[–] Wave steepness
ϵ_p	[–] Neuman's notation
$\eta_j^{(k)}$	[m] or [rad] Generalized body motions
λ	[m] Wave length
ω	[rad/s] Wave frequency
ρ	[kg/m^3] Water density
$\sigma_{p,q}$	[rad/s] Sloshing eigenfrequencies
τ	[–] Perforation ratio of the baffles
$\tilde{\sigma}_1$	[rad/s] Shifted sloshing eigenfrequency
$\varphi_{p,q}$	[–] Sloshing eigenfunction
ξ_1	[–] Damping ratio
ζ	[m] Instantaneous wave elevation
ζ_A	[m] Incident waves' amplitude
$k_{p,q}$	[rad/s] Sloshing wave number eigenvalues
v_r	[m/s] Relative flow velocity on the baffle
WP	Wave Probe

in-and-out water motions over the lid. In the current paper, we investigate the motions of a free-floating OWT's spar located inside the floating dock, with incident wave frequencies near the first natural sloshing mode. The effects of solid and perforated baffles are modeled by adapting the semi-analytical method developed for the dock alone to this new geometry.

The diffraction and radiation problems are solved in Section 2 through a domain decomposition (DD) approach, commonly used to treat geometries having a rotational symmetry. Model tests are then presented in Section 3. The semi-analytical model is extended in Section 4 to incorporate the effects of solid an perforated annular baffles in the annular domain between the dock and the spar. Results in regular and irregular waves are finally presented in Section 5.

2. Theoretical description

The geometry is presented in Fig. 1, and consists in a circular cylindrical spar inside an open-bottom cylindrical dock with bilge boxes. In later configurations, an annular baffle of width a_B and submergence d_B will be fixed to the internal wall of the dock (cf. Section 4). First, preliminary investigations on the natural sloshing eigenmodes and eigenfrequencies for the same geometry but with a closed bottom are briefly described. Then, the diffraction and radiation problems are solved by a domain decomposition approach when there is no baffle and under linear potential flow assumptions, focusing on the surge, heave and pitch motions of both bodies. Lastly, the equations of motions of the two-bodies system are discussed.

2.1. Natural sloshing modes

We first discuss sloshing eigenfunctions and eigenfrequencies in the annular domain IV between the dock and the spar, as functions of the bodies' radii. The domain IV is assumed to be closed at the bottom, and the bodies are fixed. We denote the potential eigenfunctions corresponding to the natural sloshing modes $\varphi_{p,q}$, $(p,q) \in \mathbb{N}\times\mathbb{N}^*$. Their derivation is for instance detailed in Choudhary and Bora (2017) or Faltinsen and Timokha (2016), and their analytical expressions given by:

$$\varphi_{p,q}(r,\theta,z) = \frac{b\Psi_{p,q}(r)}{\sqrt{\upsilon_{p,q}}} \frac{\cosh\left(k_{p,q}(z+d)\right)}{\cosh\left(k_{p,q}d\right)} \times \begin{cases} \cos(p\theta) \\ \sin(p\theta) \end{cases}, \tag{1}$$

where $\Psi_{p,q}$ and $\upsilon_{p,q}$ are defined such that the eigen modes are orthonormal,

$$\begin{cases} \Psi_{p,q}(r) = Y_p'(k_{p,q}a)J_p(k_{p,q}r) - J_p'(k_{p,q}a)Y_p(k_{p,q}r), \\ \upsilon_{p,q} = \left[\frac{r^2}{2}\left[1-\frac{p^2}{k_{p,q}^2r^2}\right]\Psi_{p,q}^2(r) + \frac{r^2}{2}\Psi_{p,q}'^2(r)\right]_{r=a_0}^{r=a} \end{cases}. \tag{2}$$

$\iota_{p,q} = a_0 k_{p,q}$ for $(p,q) \in \mathbb{N}\times\mathbb{N}^*$ are the roots in increasing order of:

$$J_p'(\iota_{p,q}\frac{a}{a_0})Y_p'(\iota_{p,q}) - J_p'(\iota_{p,q})Y_p'(\iota_{p,q}\frac{a}{a_0}) = 0. \tag{3}$$

J_p and Y_p are the Bessel functions of order p of the first and second kind, respectively. Only the mode $p = 1$ is linearly excited by the surge and pitch motions of the bodies, such that this index is dropped in the next sections. The roots $\iota_{p,q}$ are estimated by the algorithm proposed by Sorolla et al. (2013) which uses in an efficient manner of the interlacing properties of the Bessel functions. The first five modes are presented in Fig. 2, as well as the corresponding natural frequencies

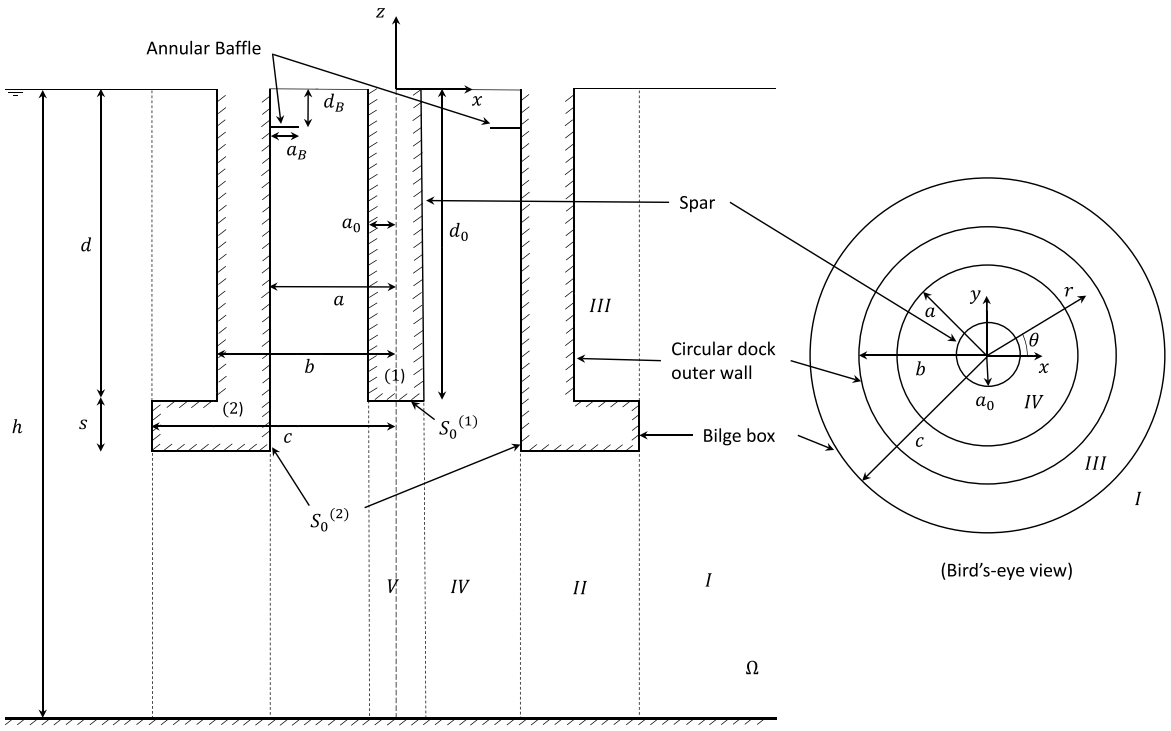

Fig. 1. Cross-section of the geometry. The spar of a floating wind turbine (body (1)) inside an upright cylindrical dock with bilge boxes (body (2)). The domain Ω is divided into five subdomains denoted I to V, and the Cartesian Earth-fixed coordinate system $Oxyz$ is defined at the free surface. h is the water depth. The mean wetted surface of the bodies are denoted S_0. A thin annular baffle is represented, fixed to the internal wall of the dock at submergence d_B and of width a_B.

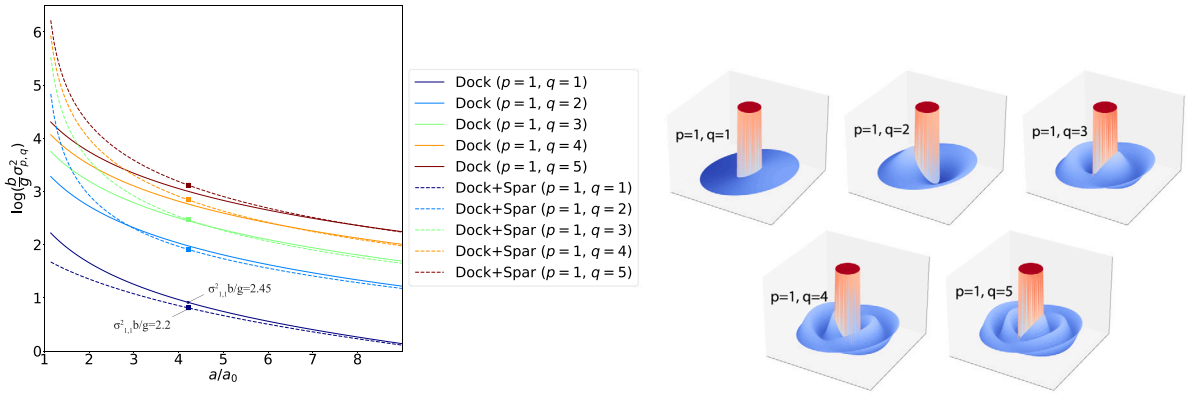

Fig. 2. Left: non-dimensional logarithmic natural sloshing frequencies of the five first modes in $p = 1$ as functions of the non-dimensional dock's radius a/a_0, the radius of the spar being fixed to $a_0/b = 0.175$. Right: shape of the five first natural sloshing modes in the annular domain. The draught is $(d + s)/b = 2$. Frequencies corresponding to actual dimensions of the dock are indicated by square points.

$\sigma^2_{p,q} = g\iota_{p,q}/a_0 \tanh(\iota_{p,q} d/a_0)$ as function of the ratio a/a_0 of the internal radius of the dock a and the spar's radius a_0.

These eigenfrequencies are compared to the case of the dock without the spar (cf. Moreau et al., 2022). It is observed that for $a/a_0 \leq 2.9$ the natural frequency of the first mode $p = 1$, $q = 1$, which is the main focus of this paper, is reduced by the presence of the spar, while natural frequencies of higher modes are increased compared to the case of the dock without spar. For the actual radius of the dock (square point on the figure), $\sigma^2_{1,1} b/g$ is around 10% lower with the spar than for the dock alone.

2.2. Domain decomposition approach

The floating dock with open bottom and the spar, as shown in Fig. 1, is now considered. The radiation and diffraction problems are tackled by a Domain Decomposition (DD) method. We consider incident regular waves of amplitudes ζ_A traveling in the positive x-direction on the dock at the frequency ω. The potential flow Φ_0 of the undisturbed incident wave is written:

$$\Phi_0 = \frac{\zeta_A g \cosh(k(z+h))}{\omega \cosh(kh)} e^{i(kr\cos(\theta)-\omega t)}, \tag{4}$$

where k is the wave number, and h the water depth. The motions of the spar (upper index $^{(1)}$) and the dock (upper index $^{(2)}$) are expressed by

$$\eta_j^{(k)} = \overline{\eta}_j^{(k)} e^{-i\omega t}, \quad j \in \{1,3,5\}, \ k \in \{1,2\}, \tag{5}$$

where $\overline{\eta}_j^{(k)}$ is the complex amplitude of the jth degree of freedom of the body (k). The total potential flow Φ in the domain Ω can be expressed as the linear combination of a scattered and radiated potentials:

$$\Phi(r,\theta,z,t) = \Phi_S + \sum_{k=1,2} \sum_{j=1,3,5} \Phi_j^{(k)}. \tag{6}$$

$\boldsymbol{\Phi}$ is harmonic in ω, and solution of the standard linear boundary value problem:

$$\nabla^2\boldsymbol{\Phi} = 0, \quad \text{in } \Omega, \tag{7}$$

$$\frac{\partial\boldsymbol{\Phi}}{\partial z} = \frac{\omega^2}{g}\boldsymbol{\Phi} \quad \text{on } z = 0, \tag{8}$$

$$\frac{\partial\boldsymbol{\Phi}}{\partial z} = 0 \quad \text{on } z = -h, \tag{9}$$

$$\frac{\partial\boldsymbol{\Phi}}{\partial n} = -i\omega\boldsymbol{\eta}^{(k)}\cdot\boldsymbol{n}^{(k)} \quad \text{on } S_0^{(k)}, k \in \{1,2\}. \tag{10}$$

$\boldsymbol{\eta}^{(k)}$ is the 6-dimensional generalized motion vector of the body (k), $\boldsymbol{n}^{(k)} = [n_1^{(k)}\ n_2^{(k)}\ n_3^{(k)}]^T$ is the unit vector pointing outward the body (k), $\boldsymbol{r} = [r\cos(\theta)\ r\sin(\theta)\ z]^T$ is the position vector, and $[n_4^{(k)}\ n_5^{(k)}\ n_6^{(k)}]^T = \boldsymbol{r}\times\boldsymbol{n}^{(k)}$. In addition, both the diffracted potential ($\boldsymbol{\Phi}_S$–$\boldsymbol{\Phi}_0$) and the radiated potentials $\boldsymbol{\Phi}_j^{(k)}$ satisfy a radiation condition far from the bodies that can be expressed as (cf. Sommerfeld, 1948): $\lim_{r\to\infty}\sqrt{kr}(\frac{\partial(\phi)}{\partial r} - ik(\phi)) = 0$.

The scattered potential $\boldsymbol{\Phi}_S$ satisfies (7)–(9) and the body-boundary condition $\frac{\partial\boldsymbol{\Phi}_S}{\partial n} = 0$ on $S_0^{(k)}, k \in \{1,2\}$. It can be decomposed in Fourier series (cf. MacCamy and Fuchs, 1954):

$$\boldsymbol{\Phi}_S(r,\theta,z,t) = -i\omega\zeta_A\sum_{p=0}^{\infty}\epsilon_p i^p\phi_p(r,z)\cos(p\theta)e^{-i\omega t}, \tag{11}$$

with $\epsilon_0 = 1$, and $\epsilon_p = 2$ for $p \in \mathbb{N}^*$. On the other hand, the radiated potentials satisfy (7)–(10) and can be written

$$\boldsymbol{\Phi}_j^{(k)} = Re[-i\omega\phi_j^{(k)}(r,z)\eta_j^{(k)}]\begin{cases}1 & \text{for } j = 3\\ \cos(\theta) & \text{for } j = 1,5\end{cases}, \tag{12}$$

where $\phi_j^{(k)}(r,z)$ describe the responses of unit forced motions in still water.

The potentials ϕ_p and $\phi_j^{(k)}$ are solved by a domain decomposition approach that takes advantage of the symmetry of revolution of the geometry. The domain Ω is divided in five vertical subdomains I to V, as defined in Fig. 1. A general solution of the Laplace equation can be expressed in each subdomain as the summation of eigen modes, weighted by unknown modal coefficients (cf. Chatjigeorgiou, 2018). The matching of normal velocities and dynamic pressures are assured by integrations over each vertical boundary common to two adjacent subdomains or by integration over the body boundaries, resulting in a linear system of equations whose resolution gives the desired potential flows. The same method was applied in Moreau et al. (2022), but in the absence of the spar. More details about the eigenfunction expansions used for geometries with this type of symmetry are for instance given by Chatjigeorgiou (2018).

In practice, the eigenfunctions' expansions must be truncated in each domain. We denote N_I to N_V the number of modes kept in the domain I to V, respectively.

Then, the total generalized force on the bodies from the diffraction problem is integrated on the surface $S_0^{(k)}$ from the dynamic pressure:

$$\boldsymbol{F}^{(k)} = -\omega^2\zeta_A\rho\sum_{p=0}^{\infty}\epsilon_p i^p\Big[\int\int_{S_0^{(k)}}\phi_p(r,z)\cos(p\theta)\,\boldsymbol{n}^{(k)}dS\Big]e^{-i\omega t}, \tag{13}$$

where ρ is the water density. Force in surge and moment in pitch are given by the mode $p = 1$ in Eq. (13), and the force in heave by the mode $p = 0$. The added mass and damping coefficients on both bodies are obtained from the radiation potentials by:

$$a_{i,j}^{(k)} = -\rho\,\Re\left[\int\int_{S_0^{(k)}}\phi_j^{(k)}\cos(p\theta)n_i^{(k)}\,\mathrm{d}S\right] \tag{14}$$

$$b_{i,j}^{(k)} = -\rho\omega\,\Im\left[\int\int_{S_0^{(k)}}\phi_j^{(k)}\cos(p\theta)n_i^{(k)}\,\mathrm{d}S\right] \tag{15}$$

$$d_{i,j}^{(k)} = -\rho\,\Re\left[\int\int_{S_0^{(k)}}\phi_j^{(k')}\cos(p\theta)n_i^{(k)}\,\mathrm{d}S\right] \tag{16}$$

$$e_{i,j}^{(k)} = -\rho\omega\,\Im\left[\int\int_{S_0^{(k)}}\phi_j^{(k')}\cos(p\theta)n_i^{(k)}\,\mathrm{d}S\right] \tag{17}$$

where $(i,j)\times(k,k') \in \{1,3,5\}^2\times\{1,2\}^2,\ k \neq k'$, and $p = 0$ in heave, and $p = 1$ in surge and pitch.

Due to the axial symmetry, there is no coupling between heave, and pitch-surge. We also observe the symmetrical properties: $a_{i,j}^{(k)} = a_{j,i}^{(k)}$, $b_{i,j}^{(k)} = b_{j,i}^{(k)}$, $d_{i,j}^{(k)} = d_{j,i}^{(k')}$, $e_{i,j}^{(k)} = e_{j,i}^{(k')}$.

Finally, the free-surface elevation is obtained from the kinematic free-surface boundary condition $\frac{\partial\zeta}{\partial t} = \frac{\partial\boldsymbol{\Phi}}{\partial z}$ in $z = 0$.

2.3. Numerical results and discussion

Results from radiation and diffraction problems were verified with the commercial boundary-element solver WAMIT (cf. Lee and Newman, 2006) for the following dimensions: $a/b = 0.75$, $c/b = 1.22$, $s/b = 0.13$, $(d+s)/b = 2$, $a_0/b = 0.18$ and $d_0/b = 2$ and $h/b = 5$ (cf. Fig. 1 for the notations). The number of modes $N_I = 50$, $N_{II} = 33$, $N_{III} = 15$, $N_{IV} = 50$, and $N_V = 33$ were found to give a good convergence between the DD method and WAMIT. Fig. 3 shows added mass and damping coefficients in surge and pitch for the dock, while Fig. 4 give the same coefficients for the spar. The damping coefficients are not shown since they are close to zero due to the deep draft of the dock. The other degrees of freedom are given in Appendix A. Several configurations are compared: the dock alone (cf. Moreau et al., 2022), the dock with open bottom and an OWT's spar inside, which is the case studied in this paper, and the spar alone in open water (OW). The sloshing resonance occurs at $\omega^2 b/g = 2.45$ for the dock alone, and is shifted to $\omega^2 b/g = 2.2$ when the spar is inserted, which correspond to the natural frequencies calculated in Section 2.1. The same resonant frequency is observed from $a_{1,1}^{(1)}$ as well as for added mass coefficients in pitch. The piston mode observed from the added mass coefficients in heave around the frequency $\omega^2 b/g = 0.4$ (cf. Appendix A) does not seem affected by the presence of the spar.

Fig. 5 presents exciting force and moment in surge and pitch on the dock. The different configurations give very similar results, especially for the dock alone and the dock with spar, which was expected.

The exciting forces, and damping coefficients on the spar were negligible because of the large draught of the dock compared to the wave length, as well as the damping coefficients on the spar. The "excitation" of the spar hence entirely came from the cross added-mass coefficients $d_{i,j}^{(1)}$, $(i,j) \in \{1,5\}^2$ caused by the dock's motions (see Appendix A), or in other words by sloshing waves.

2.4. Equations of motions

The linear equations of motions in surge and pitch are solved in frequency domain:

$$\sum_{j=1,5}[-\omega^2(M_{p,j}^{(k)} + a_{p,j}^{(k)}) - i\omega b_{p,j}^{(k)} + c_{p,j}^{(k)}]\overline{\eta}_j^{(k)} + [-\omega^2 d_{p,j}^{(k)} - i\omega e_{p,j}^{(k)} + f_{p,j}^{(k)}]\overline{\eta}_j^{(k')} = F_p^{(k)}, \quad p \in \{1,5\}^2, \tag{18}$$

where $(k,k') \in \{1,2\}^2,\ k \neq k'$, $M_{1,1}^{(k)} = M^{(k)}$ is the mass of the body (k), $M_{5,5}^{(k)} = I_{5,5}^{(k)}$ its moment of inertia in pitch, $M_{1,5}^{(k)} = M_{5,1}^{(k)} = M^{(k)}\times z_G^{(k)}$, where $z_G^{(k)}$ is the z-coordinate of the centre of gravity, and $c_{p,j}^{(k)}$ and $f_{p,j}^{(k)}$ are restoring coefficients, both hydrostatic and due to the mooring system (see Section 3).

Far from any resonance, heave motions were found to be negligible compared to the lateral motions at frequencies near sloshing resonance, and are thus disregarded hereafter.

In addition, an heuristic linearized drag load $F_D \simeq i\omega^2 8/(3\pi)C_D b(d+s)\bar{\eta}_1|\bar{\eta}_1|e^{-i\omega t}$ is added in surge for both the dock and the spar, similar to Moreau et al. (2022), with $C_D = 3$ for the dock, and $C_D = 1$ for the spar. Here, $\bar{\eta}_1$ is the surge complex amplitude.

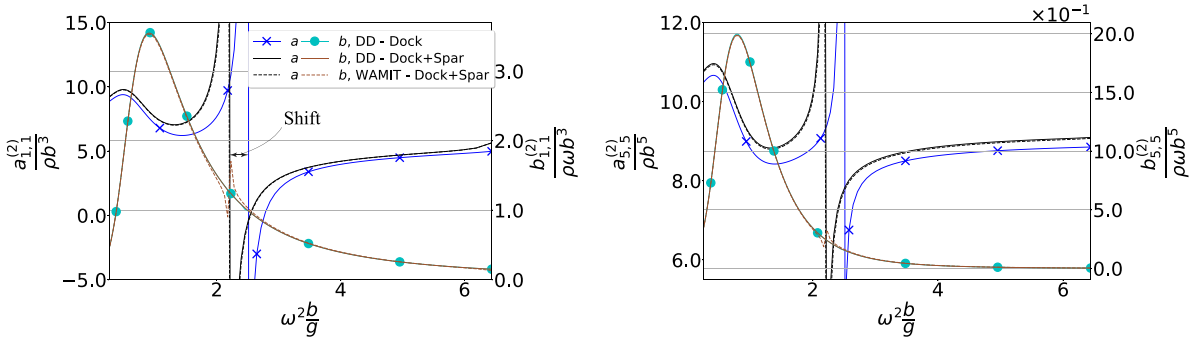

Fig. 3. Added mass and damping coefficients in surge (left) and added inertia and damping coefficients in pitch (right) of the dock. A clear shift of the natural sloshing frequency from $\omega^2 b/g = 2.45$ for the dock alone to $\omega^2 b/g = 2.2$ for the dock with spar is observed.

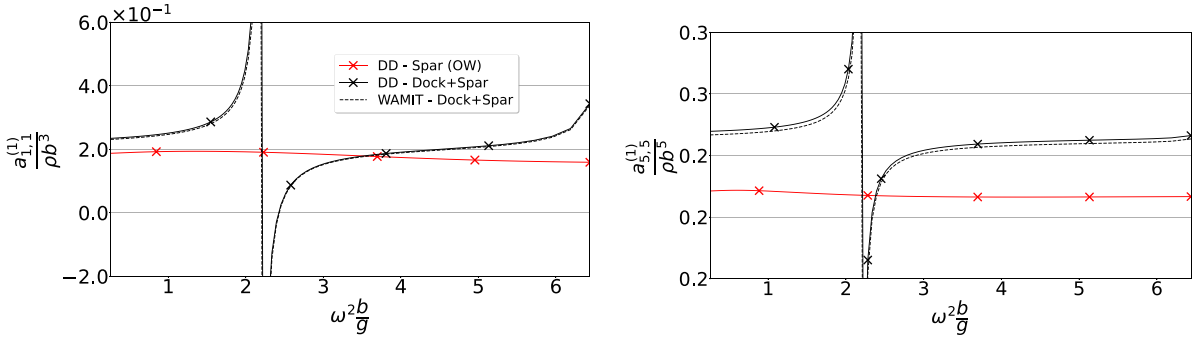

Fig. 4. Added mass coefficients in surge (left) and added inertia coefficient in pitch (right) of the spar. The case of the spar inside the dock is compared to a spar in open water (OW).

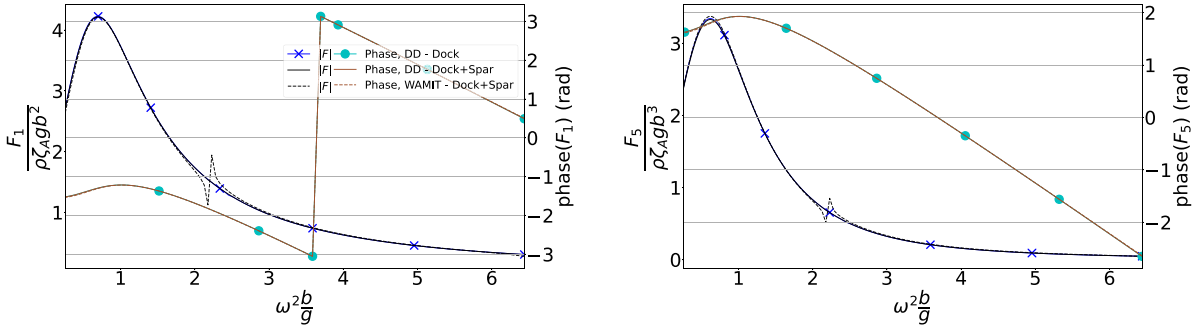

Fig. 5. Exciting forces in surge and exciting moment in pitch on the dock for the dock alone and the dock with spar. Exciting forces on the spar are negligible.

3. Model tests

3.1. Set-up of the installation

Model tests were carried out at scale 1:100 in the large towing tank at SINTEF OCEAN. Photos of the set-up are presented Fig. 6. The tank is 10.5 m wide, 85 m long and 10 m, deep, and includes a parabolic beach at its end to damp the incident waves. The dock was maintained in the middle of the tank by four external mooring lines of stiffness 120 N/m and with a pretension of about 70 N. The spar was maintained in the centre of the dock by eight mooring lines of stiffness 28 N/m: four lines at the top above the water level, four lines at the bottom. The free surface elevation was measured inside the dock near the internal wall at four different locations (denoted WP1 to 4), and outside the dock, both in front of the model (WP5 and WP8) and on its two lateral sides (WP6 and WP7), as shown on Fig. 7. The rigid-body motions of both bodies were captured by two independent video positioning systems. Three accelerometers were also installed on the top of the dock to measure its surge, heave and pitch accelerations, providing more control on the dock's motions. These last measurements were privileged in the result section due to the higher precision of the accelerometers compared to the video positioning system.

Details about the geometry and mass of the two bodies are given in Table 1. Several tests included solid and perforated baffles with a perforation ratio $\tau = 0.3$ with $\tau =$ open area/total area. The baffles were rigidly fixed 0.05 m below the mean free surface on the interior wall of the dock. The width of the baffles was $a_B = 0.05$ m, and thickness 0.005 m. The scale effects when the baffles are installed are not expected to be significant, since it is known that the flow separation occurs at the sharp edge of the baffle.

Free decay experiments were performed for the dock with the spar in various degrees of freedom in order to roughly estimate natural periods of the coupled system. Natural periods of the dock were similar as for the dock alone: $T_N = 11$ s in surge, 2.3 s in both heave and pitch. For the spar it was measured: $T_N = 1.3$ s in pitch and 1.5 s in heave. Free decays in surge could not be performed for the spar because of the strong coupling with pitch and heave.

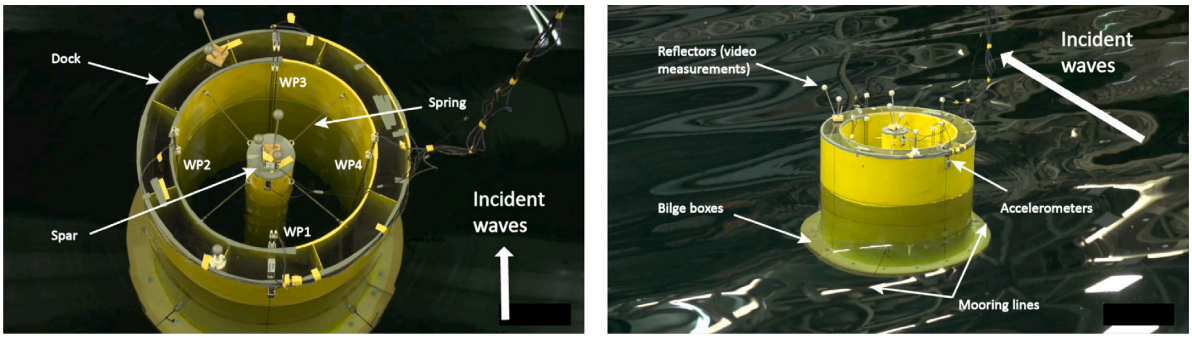

Fig. 6. Photos from the model tests carried out at SINTEF OCEAN. Left: top view of the installation, the spar is maintained in the centre of the dock by eight mooring lines, four at the top (observable on the first photo) and four at the bottom. Four wave probes are mounted near the dock's internal wall. Right: side view, two distinct video positioning systems measure the motions of the dock and the spar.

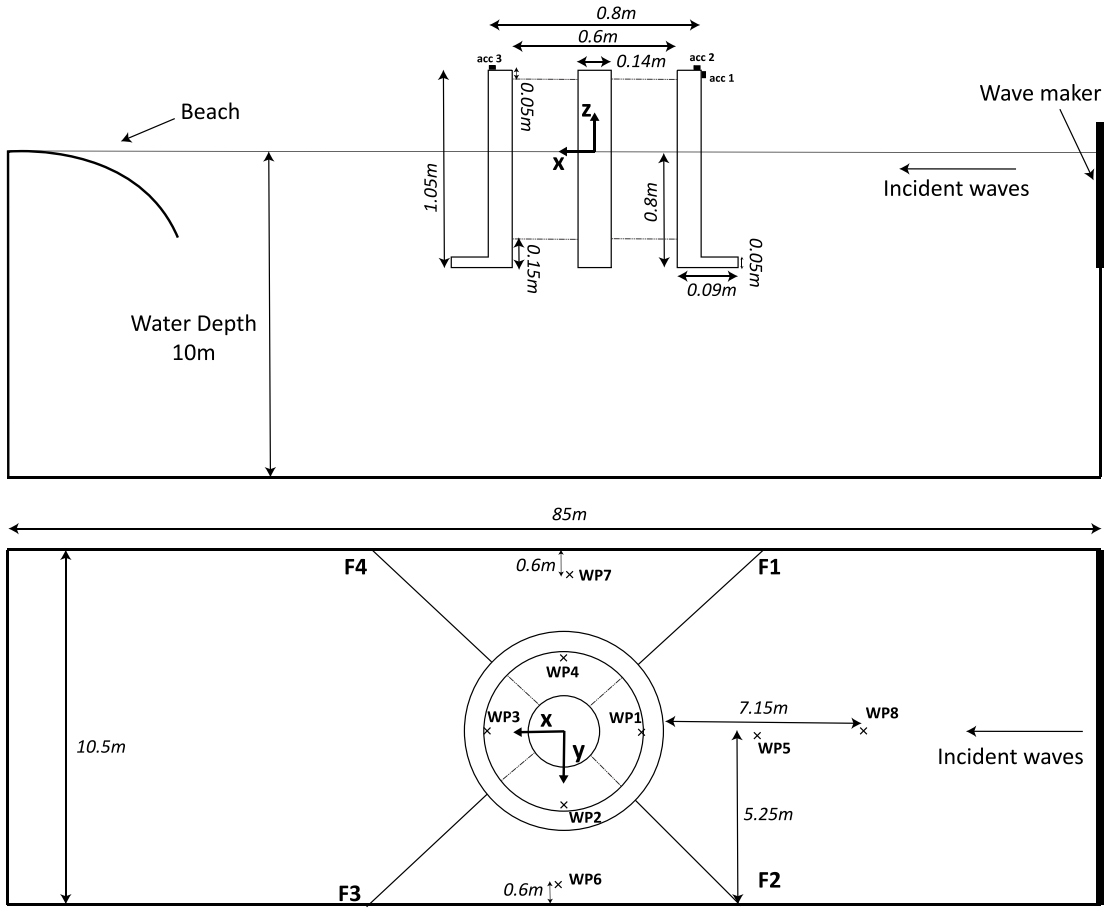

Fig. 7. Side and bird's-eye views of the experimental set-up (not to scale). The four wave probes WP1 to 4 are fixed to the dock, and WP5 to WP8 are fixed to the tank.

These natural periods were generally higher than the sloshing natural period $T_1 = 0.85$ s (i.e. $\omega^2 b/g = 2.2$), but close to the piston mode $T_{piston} = 2$ s (i.e. $\omega^2 b/g = 0.4$, cf. Section 2.3), which is not investigated in this paper.

3.2. Tests in regular waves

Regular waves were generated in the tank, with periods near sloshing resonance. Repetition tests were made for the case without baffle to evaluate random errors. The root mean square deviations between the response amplitude operator (RAO) of the repetition tests were found to be in a range from 1 to 5% for the dock's motion, and 7 to 11% for the spar's motions and free-surface elevation inside the dock.

The wave steepness $\epsilon = 2\zeta_A/\lambda = 1/60$ was kept constant. $\epsilon = 1/45$ and $1/30$ were also considered for the case without baffle. The signal processing in regular waves was described by Moreau et al. (2022), and is not repeated here. Examples of time histories of $\eta_1^{(1)}$, $\eta_1^{(2)}$ and ζ_{WP1} are presented in Fig. 8 with and without baffle for two incident wave periods, below and above the natural sloshing period. In particular, it shows that the transient states of the signals before they reach steady states are much reduced when the baffle is installed, especially the solid baffle, due to higher viscous damping. Without baffle, steady states were only reached after approximatively 30 s. Beating was observed for low incident wave periods below $T = 0.7$ s. As expected, ζ_{WP1} and ζ_{WP3} were in opposition of phase with similar amplitudes, while ζ_{WP2} and ζ_{WP4}, measured from the transverse wave probes inside the dock, were generally negligible. Only for low wave periods ζ_{WP2} and ζ_{WP4} were

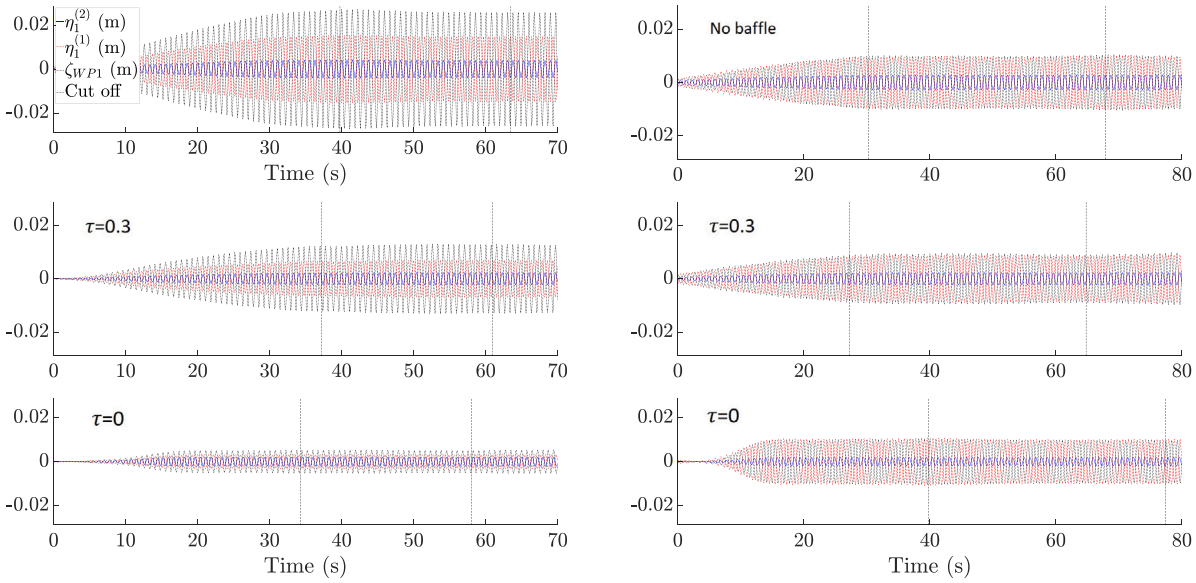

Fig. 8. Time series of $\eta_1^{(1)}$, $\eta_1^{(2)}$ and ζ_{WP1} without baffle (top), with perforated baffle (middle) and solid baffle (bottom), and for two incident wave periods: $T = 0.74$ s, or $\omega^2 b/g = 2.94$ (left) and $T = 0.9$ s, or $\omega^2 b/g = 1.99$ (right). The part of the signals being post-processed are in between the cut-off delimiters. Wave steepness: $\epsilon = 1/60$.

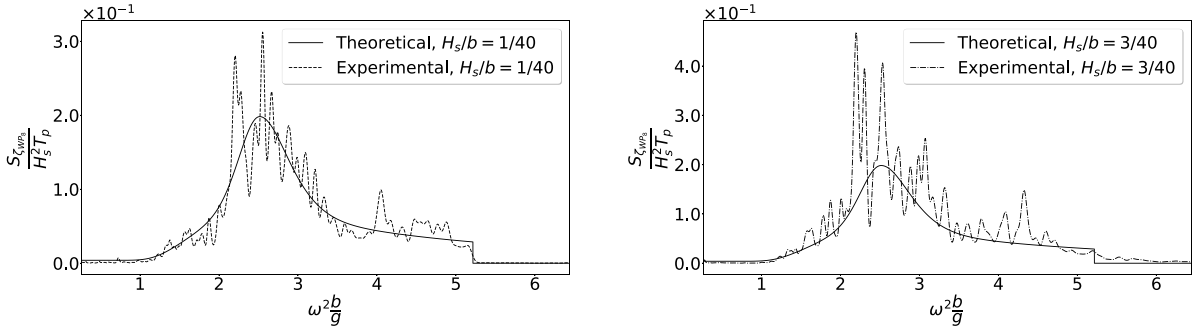

Fig. 9. JONSWAP spectra of incident waves, as instructed to the command of the wave maker (theoretical), and measured in front of the model at the wave probe ζ_{WP8} with the model in place (experimental).

Table 1
Dimensions and mass properties of both the dock and the SPAR - Notations referring to the geometry are defined in Fig. 1. M is the mass of each body, $I_{5,5}$ the moment of inertia, and z_G the centre of gravity.

Parameter	Unit	Value
a	[m]	0.30
b	[m]	0.40
$d + s$	[m]	0.80
s	[m]	0.05
$c - b$	[m]	0.09
a_0	[m]	0.07
d_0	[m]	0.80
a_B	[m]	0.05
d_B	[m]	0.05
$z_G^{(1)}/z_G^{(2)}$	[m]	−0.5/−0.52
$I_{5,5}^{(1)}/I_{5,5}^{(2)}$	[kg m^2]	4.3/78
$M^{(1)}/M^{(2)}$	[kg]	12.3/188.3

non-negligible, reaching near 30% the amplitude of ζ_{WP1}. Swirling was also observed for very few tests, also at low periods, and characterized by a difference of phase of 90deg between the four wave probes.

3.3. Tests in irregular waves

Test with irregular waves were performed for the dock with spar and without baffle. The irregular waves were characterized by standard JONSWAP spectra defined by their peak period $T_p = 0.8$ s (corresponding to a peak frequency $\omega_p^2 b/g = 2.52$), their peak enhancement coefficient $\gamma = 3$ and their significant wave height H_s. Two values of H_s were tested, $H_s/b = 1/40$ and $H_s/b = 3/40$. The spectra of incident waves, both theoretical and measured, are presented in Fig. 9. Each test in irregular waves was 10 min long. The measured spectra were band-pass filtered for a range of periods containing 98% of the energy from the theoretical wave spectra, and then smoothed by a standard Gaussian filter. Fig. 10 presents part of time series of $\eta_1^{(1)}$, $\eta_1^{(2)}$ and ζ_{WP1} in irregular waves for $H_s/b = 1/40$.

4. Annular baffles

Annular baffles fixed on the internal wall of the dock (cf Fig. 1) are characterized by their width a_B, submergence d_B, and perforation ratio τ. The effects of the baffle are included in the semi-analytical model in the same manner as in Moreau et al. (2022) to account for the flow separation. This method is based on a single mode approximation to represent the sloshing wave inside the dock, and aims to reproduce the

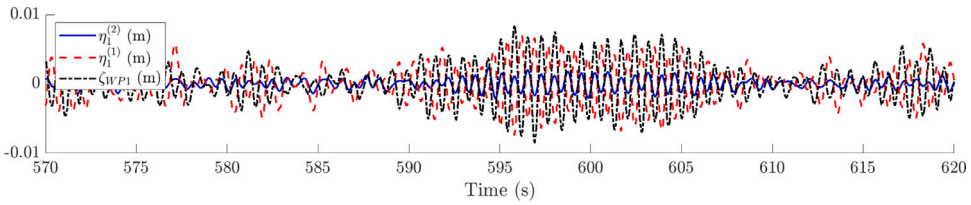

Fig. 10. Time series of $\eta_1^{(1)}$, $\eta_1^{(2)}$ and ζ_{WP1}. $H_s/b = 1/40$.

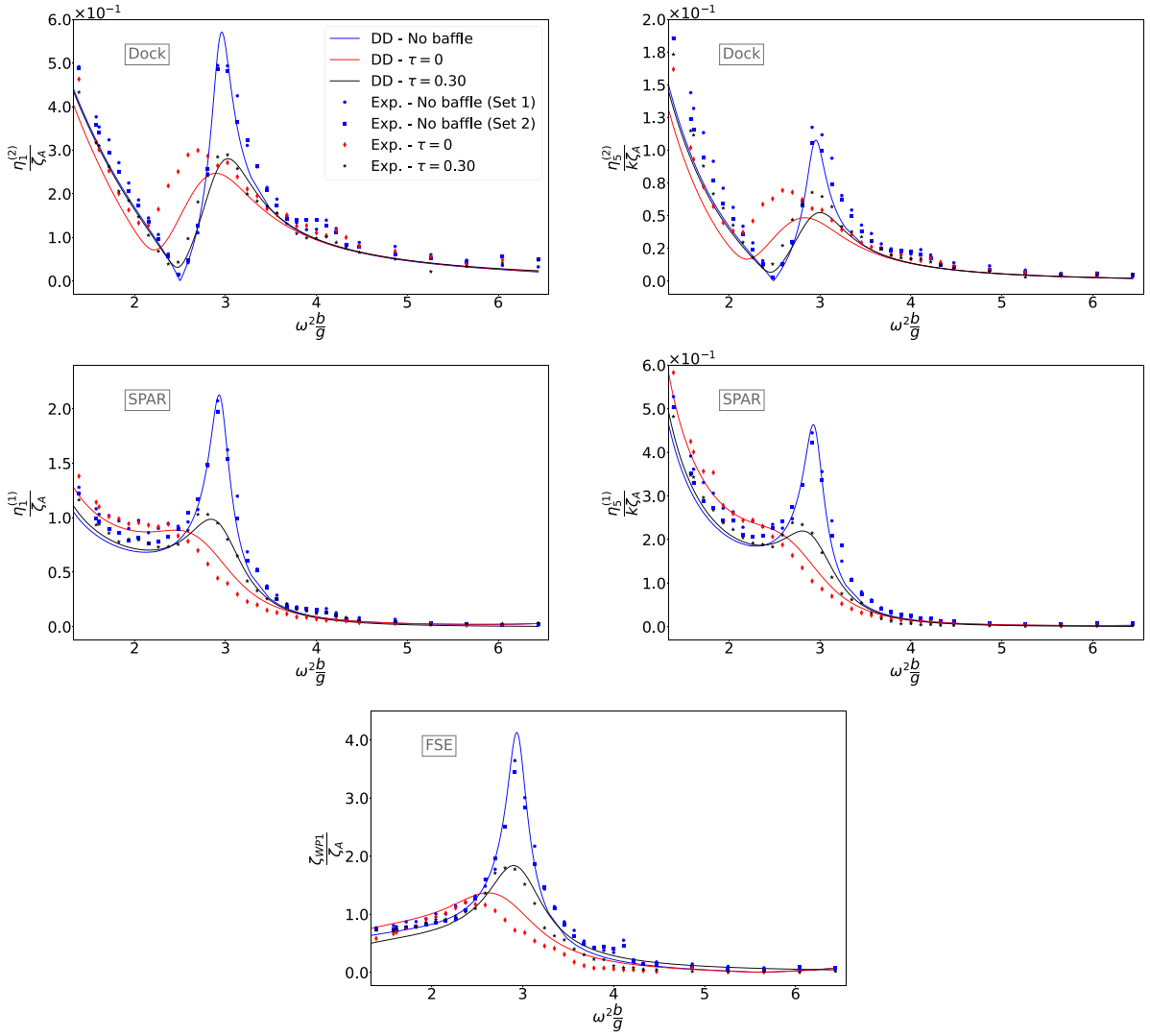

Fig. 11. RAOs of the dock's and spar's motions, and of the free-surface elevation (FSE) inside the dock at $WP1$. Experimental and analytical results are compared for cases without baffle (sets 1 and 2), with a solid annular baffle ($\tau = 0$) and perforated baffle ($\tau = 0.3$). Two experimental repetition tests are compared for the cases without baffle. Wave steepness: $\epsilon = 1/60$.

two main effects of the baffles: the reduction of the natural sloshing frequency, and the quadratic viscous dissipation. It is assumed that the presence of the baffle does not affect the flow motions at the bottom of the dock.

Although the method is similar to Moreau et al. (2022), the eigen sloshing modes are changed by the presence of the spar inside the dock, in particular the first natural frequency is reduced. Furthermore, the motions of both bodies are now exciting sloshing waves.

Under first mode approximation, the summation of the radiation potentials in Section 2.2 in the domain IV between the dock and the spar are written as:

$$\Phi(r,\theta,z,t) = \sum_{\substack{k\in\{1,2\}\\ j\in\{1,5\}}} \Phi_j^{(k),RFS}(r,\theta,z,t) + R(t)\varphi_1(r,\theta,z), \tag{19}$$

where $\Phi_j^{(k),RFS}$ satisfies the Eqs. (7), (9), (10), and the "rigid free-surface" (RFS) condition $\dfrac{\partial \Phi_j^{(k),RFS}}{\partial z} = \eta_j^{(k)} n_5^{(2)}$ on $z = 0$, while the eigen mode φ_1 assures the free surface boundary condition Eq. (8) in a dock-fixed coordinate system. $R(t)$ is a time dependent constant. $\Phi_j^{(k),RFS}$ can be expressed similar to Eq. (12) and solved through a DD method, assuring the matching conditions with external domains.

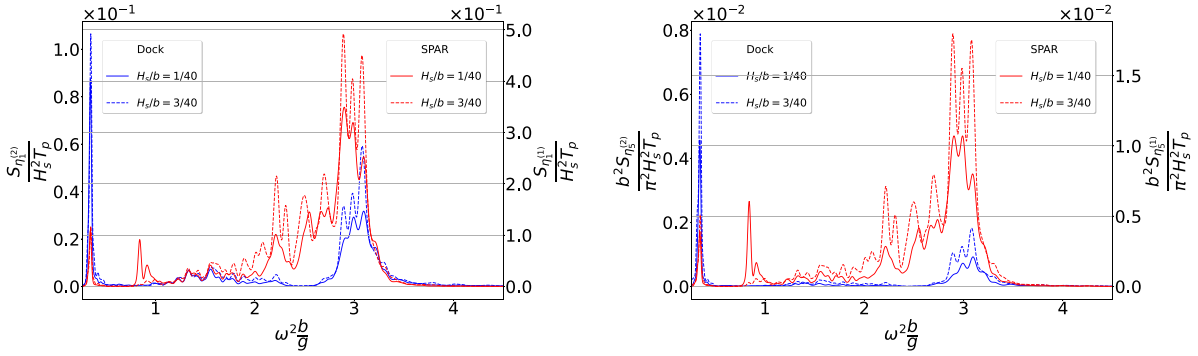

Fig. 12. Normalized spectra of the dock's and spar's responses in surge (left) and pitch (right) motions from model tests, for two different sea-states in an Earth-fixed coordinate system.

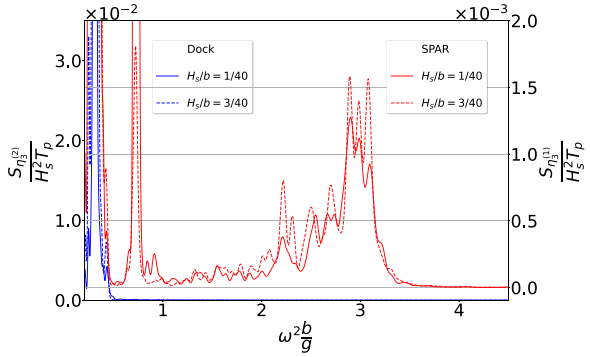

Fig. 13. Normalized spectra of the dock's and spar's responses in heave in an Earth-fixed coordinate system.

The free-surface inside the dock is given under single-mode approximation and in a dock-fixed coordinate system by:

$$\zeta(x,y,t) = \beta(t)\varphi_1(x,y,0), \tag{20}$$

and the modal equations are established for β_1 and R_1 by inserting the expressions (19) and (20) in the dynamic and kinematic free-surface boundary conditions for Φ:

$$\dot{\beta}_1 = \frac{\tilde{\sigma}_1^2}{g} R_1, \tag{21}$$

$$\ddot{\beta}_1 + 2\xi_1\tilde{\sigma}_1\dot{\beta}_1 + \tilde{\sigma}_1^2\beta_1 = K_1(t). \tag{22}$$

$K_1(t) = \tilde{P}_i^{(k)}\ddot{\eta}_i^{(k)}$ is a motion-dependent excitation term, derived from the potentials $\Phi_j^{(k),RFS}$. The details of the calculations are given in Appendix B. An equivalent linear damping ratio ξ_1 is included to account for the viscous dissipation, and $\tilde{\sigma}_1$ is the natural sloshing frequency, which is reduced compared to σ_1 due to the baffle. The methods used to estimate ξ_1 and $\tilde{\sigma}_1$ are detailed in Moreau et al. (2022) for the case without spar, and are not repeated here. One of the major difference with fully closed domains as in Faltinsen and Timokha (2009), is that the $\tilde{P}_i^{(k)}$ coefficients depend now on the forcing frequency ω of the incident waves, and not only on the geometry of the domain. It would for example become more complicated to solve the modal equations in time domain.

The steady-state solution of the modal equations is given in frequency domain by:

$$R_1(t) = \frac{g}{\sigma_1^2}\frac{i\omega K_1(t)}{2i\omega\sigma_1\xi_1 + \omega^2 - \sigma_1^2} = f_1(\omega)K_1(t), \tag{23}$$

Added mass and damping coefficients due to the potentials $\Phi_j^{(k),RFS}$ and calculated from the DD approach are expressed similar to Eqs. (14) to (17), replacing $\phi_j^{(k)}$ by $\phi_j^{(k),RFS}$ in each equation. Added mass and damping coefficients due to the first-mode-approximated sloshing wave $R(t)\varphi_1$, which account for the effects of the baffle, are given by:

$$a_{i,j}^{(k)\text{slosh}} + \frac{i}{\omega}b_{i,j}^{(k)\text{slosh}} = i\omega g_i^{(k)} f_1(\omega)\tilde{P}_j^{(k)}(\omega), \tag{24}$$

$$e_{i,j}^{(k)\text{slosh}} + \frac{i}{\omega}d_{i,j}^{(k)\text{slosh}} = i\omega g_i^{(k)} f_1(\omega)\tilde{P}_j^{(k')}(\omega), \tag{25}$$

where $(j,k) \in \{1,5\}^2, (k,k') \in \{1,2\}^2,\ k \neq k'$, and $g_j^{(k)} = \rho \int\int_{S_0^{(k)}} \varphi_1 n_j^{(k)} \mathrm{d}S$.

The bodies' motions are first needed to determine $\tilde{\sigma}_1$ and ξ_1. A first iteration is hence simulated without baffle, and an iterative scheme is implemented until convergence of the bodies' motions.

In the case a baffle is installed inside the dock, the added mass and damping coefficients include the terms (24) and (25), and the pitch moment on the dock

$$F_5^M = -\int_0^{2\pi} a\left[\frac{1}{2}\rho\, a_B\, C_D\, v_r|v_r| + \frac{1}{4}\rho\pi a_B^2 C_M \frac{\partial v_r}{\partial t}\right]\cos(\theta)d\theta, \tag{26}$$

integrated from the two-dimensional Morison load on the baffle (cf. Graham, 1980), is added to the left hand side of the equations of motions.

5. Results

The RAOs of the bodies' motions and the free-surface elevation inside the dock are presented in an Earth-fixed coordinate system. Analytical and experimental results are first compared in regular waves, then in irregular waves.

5.1. Regular waves

RAOs in regular waves are presented in Fig. 11 for the dock and spar, including results with an annular baffle fixed inside the internal wall of the dock, either solid ($\tau = 0$) or perforated ($\tau = 0.3$). The motions of the dock are almost null at the natural sloshing frequency $\sigma_1^2 b/g = 2.5$ for the case without baffle, due to the drastic increase of the added mass at this frequency. The maximum amplitudes of the dock's and spar's motions are obtained numerically around the frequency $\omega^2 b/g = 2.95$. For the case without baffle, analytical results are fairly consistent with the experimental ones. The highest discrepancies are observed for the surge and pitch motions of the dock, and might be caused by inaccuracies when modeling the inertial and stiffness matrices of the dock for the semi-analytical model. Heave motions were negligible at these wave periods, and are not presented here. $\eta_3^{(1)}/\zeta_A$ motion was for example around 15 times lower than $\eta_1^{(1)}/\zeta_A$, even though a resonant peak was also observed in the experiments at the same frequency, suggesting slight non-linear motions of the spar, and suspected to be caused by the mooring installation between the spar and the dock.

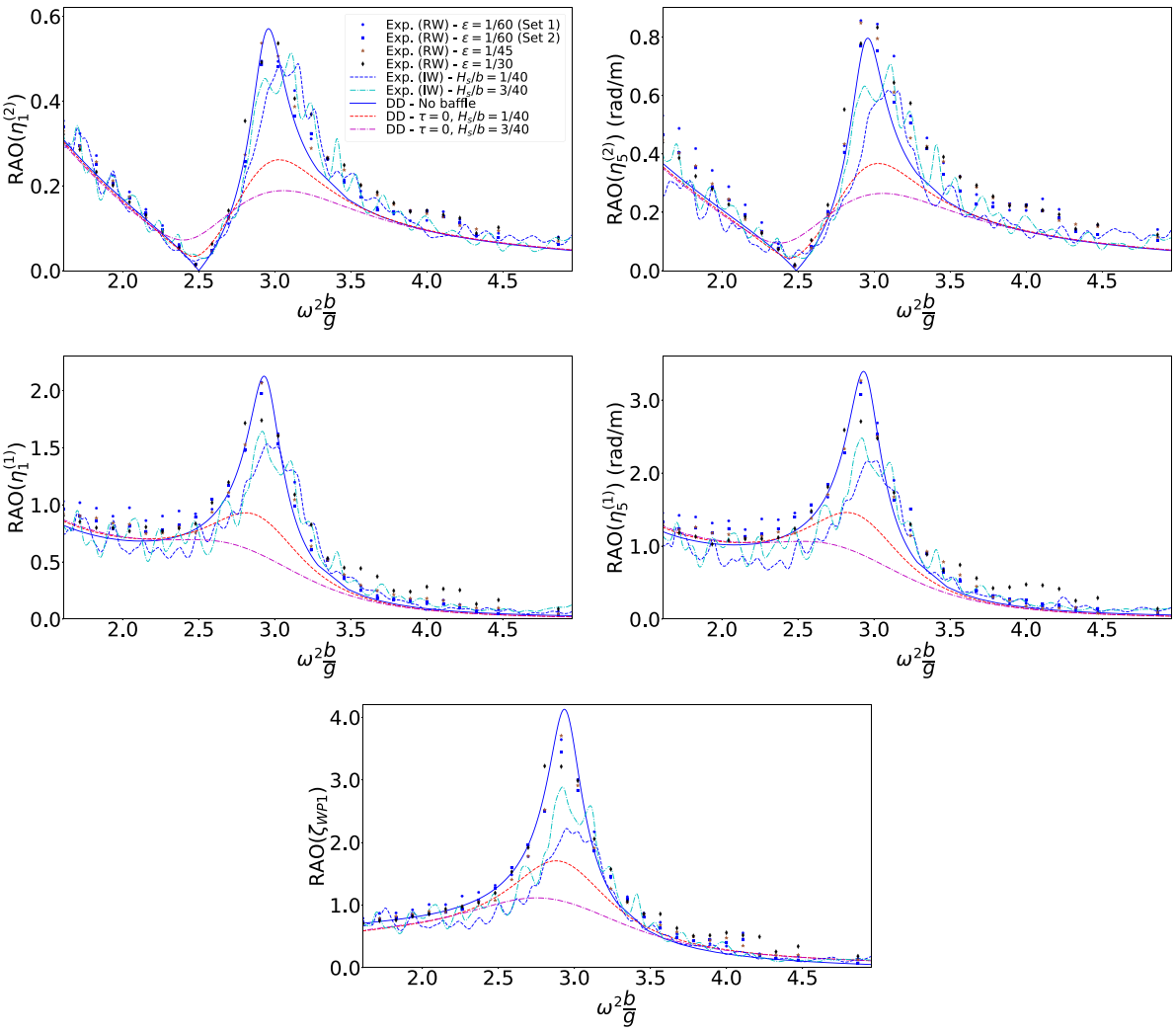

Fig. 14. Analytical and experimental RAOs for regular waves (RW) and irregular waves (IW) without baffle, and with solid baffle (DD only) for different sea-states.

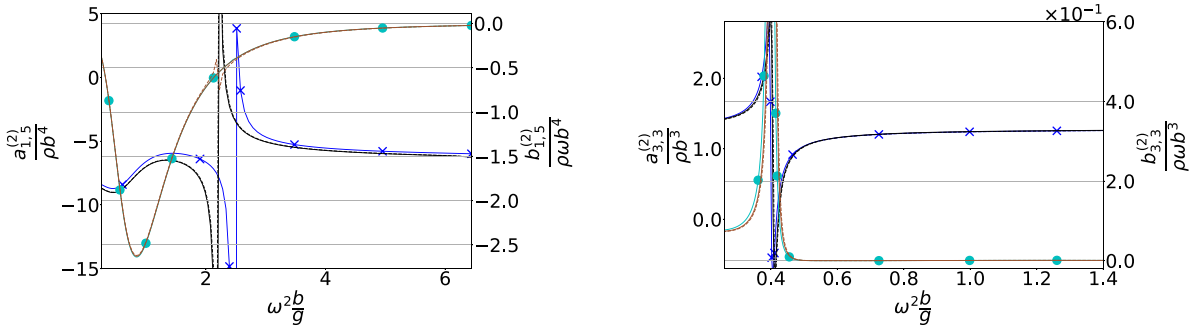

Fig. 15. Added mass and damping coefficients on the dock for the two bodies system dock & spar. The legend is given in Fig. 3.

The baffles, both solid and perforated, have a major influence on the responses. The reduction of the peak amplitude when comparing with the case without baffle is particularly important for the spar motions and free-surface elevation. With a solid baffle this reduction is around 54% for $\eta_1^{(1)}/\zeta_A$, 45% for $\eta_1^{(5)}/\zeta_A$ and 68% for ζ_{WP1}/ζ_A (from experimental RAOs). The frequency for which the maximum peak amplitudes are reached is different for the dock, and spar's motions, around 10% lower for the latter.

The analytical results catch the shift of the natural sloshing frequency due to the baffles, and compare relatively well with the spar's experimental motions. However, the motions of the dock are underpredicted and the resonant peak frequency is about 6% higher than the experimental one. These discrepancies were not as high for the dock without spar (cf. Moreau et al., 2022). As in our previous paper, the shape of the first sloshing mode φ_1 does not account for the baffle in our model. We suspect that this assumption brings errors

when calculating the local loads on the dock. Non-linear free-surface interaction associated with the baffle are also expected.

Baffle with a perforation ratio $\tau = 0.3$ are not as efficient in damping the sloshing waves, with 51% reduction of ζ_{WP1}/ζ_A's peak amplitude. However, they show similar performances to the solid baffle when it comes to reduce the spar's motions' peak amplitude: 50% for $\eta_1^{(1)}/\zeta_A$, 46% for $\eta_5^{(1)}/\zeta_A$. Discrepancies for the dock's motions between analytical and experimental results are less pronounced.

5.2. Irregular waves

Power spectra of the responses in surge and pitch are presented in Fig. 12 for irregular sea-states for the dock and spar without baffle. Energy of the bodies' motions is concentrated around the peak resonance observed in regular waves around $\omega_1^2 b/g = 2.95$. The energy of the heave motions for frequencies higher than $\omega^2 b/g = 1$ is less than 0.5% of that in surge for both bodies, as seen in Fig. 13, confirming that non-linear excitation of these motions were negligible in that range. Resonance of the spar's heaving was observed near $\omega^2 b/g = 0.75$, which was also measured from decay tests, and suspected to excite the spar's pitch motion due to non-linear coupling from the mooring fixation of the spar.

Fig. 14 shows experimental RAOs in irregular waves without baffle, compared with semi-analytical results. Experimental results are significantly lower than semi-analytical ones for all the motions. Based on our investigations, this is most likely due to the long transient state that characterizes responses with very low damping, preventing the sloshing responses to develop entirely. The experimental RAOs for $H_s/b = 1/40$ and $H_s/b = 3/40$ for the tests without baffle are very similar, and within the range of random uncertainty. This is consistent with the regular wave tests, shown on the same figure for several wave steepnesses, including repetition tests for $\epsilon = 1/60$.

Calculated results with a solid annular baffle are also presented in Fig. 14 for both irregular sea-states. The Morison load (26) on the baffle was stochastically linearized (cf. Wolfram, 1999), as well as the heuristic damping in surge given in Section 2.4 for the dock and the spar. The damping ratio and shifted sloshing natural frequency introduced in Eq. (22) were considered constant over the range of frequencies that was simulated, evaluated from the highest wave amplitudes measured in experimental time series. This last assumption is quite approximative for ξ_1, which is strongly dependent on the incident wave amplitude, but is expected to provide a relatively safe estimation of $\tilde{\sigma}_1$, which was shown to vary less than 1% over the spectra in regular waves. Unlike the case without baffle, the motions are highly dependent on H_s/b due to non-linearities. The reduction of the spar's motions are significant for both sea-sates at the resonant peak, from 35%–40% for $H_s/b = 1/40$ to 50%–55% for $H_s/b = 3/40$ compared to the case without baffle.

The high reduction of the body's motions at the resonant peak due to the baffle is consistent with the results observed in regular waves (cf. Fig. 11). Either with or without baffle, the maximum responses of the spar are near four times higher than the maximum responses of the dock, and dominate the relative motions between both bodies. Further studies on the relative motions between the dock and the OWT at different stages of the assembly are left for dedicated future work.

6. Conclusions

The motions in surge and pitch of a free-floating OWT's spar inside a moored cylindrical dock with open bottom were investigated near sloshing resonance both analytically and experimentally. A semi-analytical model based on domain decomposition was further developed. The effects of solid and perforated annular baffles were implemented locally in the free-surface boundary condition in the domain between the spar and the dock, extending the semi-analytical model at very low computational costs. Results in regular waves showed a good agreement with experimental values. Both solid and perforated baffles caused significant reductions of the spar's motions at resonance for low wave steepnesses. Motions in irregular sea states were significantly over-predicted by the semi-analytical model, most likely due to the long transient phases observed in time domain before reaching steady states, and not caught by the frequency-domain solver.

The spar's motions were shown very sensitive to its mass distribution. Further work could for example include different stages of the assembly of the OWT. Sea-keeping of the dock at more extreme sea-states should also receive a special attention, since the piston mode and heave resonances are expected to be non-negligible at lower incident wave frequencies.

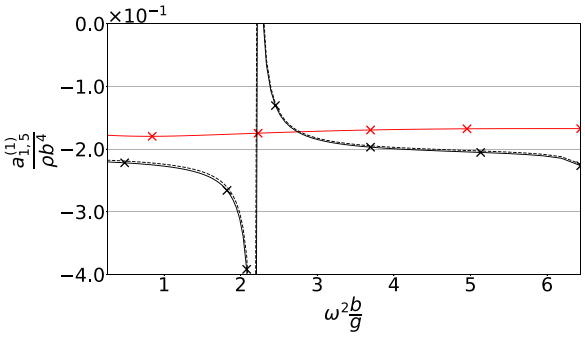

Fig. 16. Added mass coefficients on the spar for the two bodies system dock & spar. The legend is given in Fig. 4.

Declaration of competing interest

The authors declare that they have no known competing financial interests or personal relationships that could have appeared to influence the work reported in this paper.

Data availability

Data will be made available on request.

Acknowledgments

This work was financially supported by the Research Council of Norway through the Centre for Research-based Innovation of Marine Operations (SFI MOVE).

Appendix A

Fig. 15 shows added mass and damping coefficients $a^{(2)}$ and $b^{(2)}$ on the dock, in complement of Section 2.3. Added mass and damping coefficients $a_{1,5}^{(1)}$ and $b_{1,5}^{(1)}$ on the spar, and coupled coefficients $d^{(1)}$ and $e^{(1)}$ between the dock and the spar (cf. Eqs. (16) and (17)) are given by Figs. 16 and 17, respectively.

Appendix B

The exciting coefficient $K_1(t)$ in the modal equation Eq. (23) is given by:

$$K_1(t) = -\frac{1}{\mu_1}\left[\lambda_{1,1}^{(1)}\ddot{\eta}_1^{(1)} + \lambda_{1,1}^{(2)}\ddot{\eta}_1^{(2)} + \lambda_{1,5}^{(1)}\ddot{\eta}_5^{(1)} + \lambda_{1,5}^{(2)}\ddot{\eta}_5^{(2)} - \Lambda_{1,5}g\eta_5^{(2)}\right], \quad (27)$$

where

$$\mu_1 = \frac{\rho g}{\tilde{\sigma}_1^2}\int_{\Sigma_0}\varphi_1(r,\theta,0)^2 r d\theta dr, \quad (28)$$

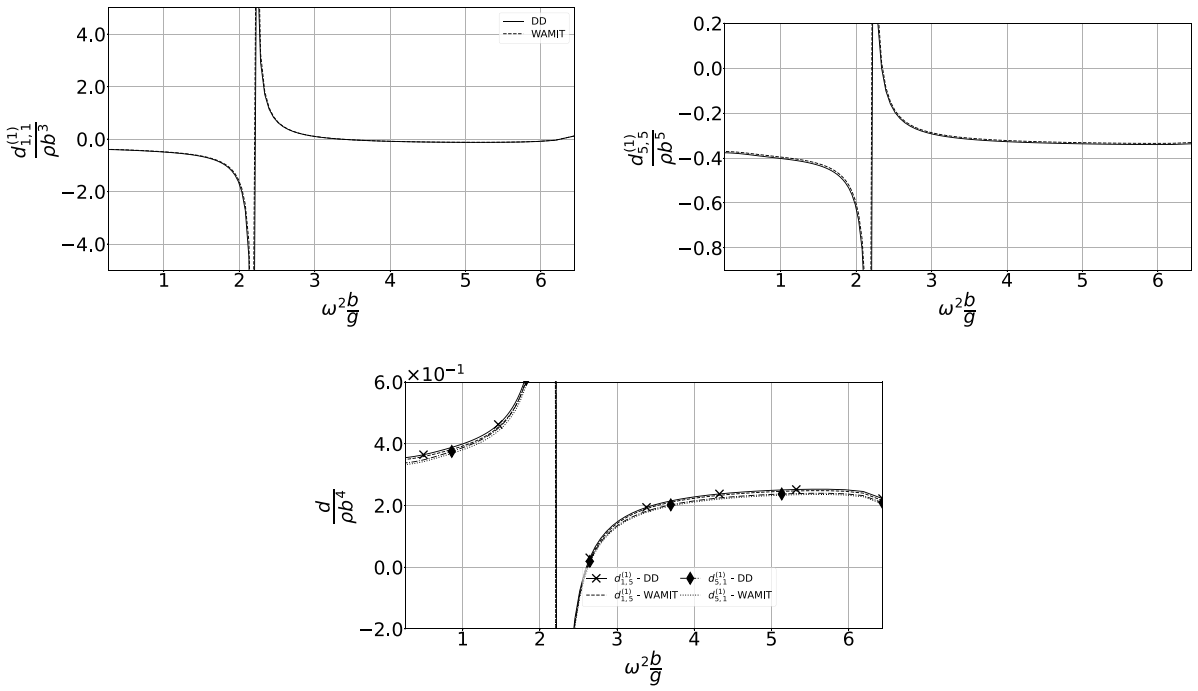

Fig. 17. Added mass coefficients, cross coefficients - Two bodies system dock & spar.

$$\lambda_{1,j}^{(k)} = \rho \int_{\Sigma_0} \phi_j^{(k),RFS}(r,0)\cos(\theta)\varphi_1(r,\theta,0) r d\theta dr, \quad (j,k) \in \{1,5\} \times \{1,2\}, \tag{29}$$

$$\Lambda_{1,5} = \rho \int_{\Sigma_0^{(2)}} r\cos(\theta)\varphi_{1,1}(r,\theta,0) r d\theta dr = \frac{\rho\pi}{\sqrt{v_{1,1}}} \int_{a_0}^{a} \Psi_{1,1}(r) r^2 dr. \tag{30}$$

References

Chatjigeorgiou, I., 2018. Analytical Methods in Marine Hydrodynamics. Cambridge University Press.

Choudhary, N., Bora, S., 2017. Linear sloshing frequencies in the annular region of a circular cylindrical container in the presence of a rigid baffle. Sādhanā 42, 805–815.

Faltinsen, O.M., Timokha, A., 2009. Sloshing, first ed. Cambridge University Press.

Faltinsen, O.M., Timokha, A., 2016. Resonant sloshing in an upright annular tank. J. Fluid Mech. 804, 608–645.

Graham, J., 1980. The forces on sharp-edged cylinders in oscillatory flow at low Keulegan-Carpenter numbers. J. Fluid Mech. 97, 331–346.

International Energy Agency (IEA), 2019. Offshore wind outlook 2019. [online]. Available from: https://www.iea.org/reports/offshore-wind-outlook-2019 [Accessed 15 August 2022].

Jiang, Z., Yttervik, R., Gao, Z., Sandvik, P., 2020. Design, modelling, and analysis of a large floating dock for spar floating wind turbine installation. Mar. Struct. 72.

Lee, C., Newman, J., 2006. WAMIT user manual, versions 6.3, 6.3pc, 6.3s, 6.3s-PC.

MacCamy, R., Fuchs, R., 1954. Wave Forces on Piles: A Diffraction Theory. Tech. Memo. 69, U.S. Army Corps of Engineers Beach Erosion Board.

Moreau, M., Kristiansen, T., Ommani, B., Molin, B., 2022. An upright bottomless vertical cylinder with baffles floating in waves. Appl. Ocean Res. 119.

Shukla, P., Skea, J., Slade, R., Al Khourdajie, A., Van Diemen, R., McCollum, D., Pathak, M., Some, S., Vyas, P., Fradera, R., Belkacemi, M., Hasija, A., Lisboa, G., Luz, S., Malley, J., 2022. IPCC, 2022: Mitigation of Climate Change. Contribution of Working Group III to the Sixth Assessment Report of the Intergovernmental Panel on Climate Change. Cambridge University Press, Cambridge, UK and New York, NY, USA.

Skaare, B., 2017. Development of the hywind concept. In: Proceedings of the ASME 2017 36th International Conference on Ocean, Offshore and Arctic Engineering, Trondheim, Norway.

Sommerfeld, A., 1948. Vorlesungen über theoretische physik. Leipz. Akd. Verl. 69.

Sorolla, E., Mosig, J.R., Mattes, M., 2013. Algorithm to calculate a large number of roots of the cross-product of bessel functions. IEEE Trans. Antennas and Propagation 61, 2180—2187.

Wolfram, J., 1999. On alternative approaches to linearization and Morison's equation for wave forces. Proc.: Math. Phys. Eng. Sci. 455, 2957—74.

Yue, H., Jianyun, C., Xu, Q., 2018. Sloshing characteristics of annular tuned liquid damper (ATLD) for applications in composite bushings. Struct. Control Health Monit. 25.